Journal of Geophysical Research: Space Physics

RESEARCH ARTICLE
10.1029/2018JA025391

# Interchange Injections at Saturn: Statistical Survey of Energetic $H^+$ Sudden Flux Intensifications

**Abigail R. Azari[1], Michael W. Liemohn[1], Xianzhe Jia[1], Michelle F. Thomsen[2], Donald G. Mitchell[3], Nick Sergis[4,5], Abigail M. Rymer[3], George B. Hospodarsky[6], Christopher Paranicas[3], and Jon Vandegriff[3]**

[1]Department of Climate and Space Sciences and Engineering, University of Michigan, Ann Arbor, MI, USA, [2]Planetary Science Institute, Tucson, AZ, USA, [3]Applied Physics Laboratory, The Johns Hopkins University, Laurel, MD, USA, [4]Office of Space Research and Technology, Academy of Athens, Athens, Greece, [5]Institute for Astronomy, Astrophysics, Space Applications and Remote Sensing, National Observatory of Athens, Penteli, Greece, [6]Department of Physics and Astronomy, University of Iowa, Iowa City, IA, USA

**Key Points:**
- We developed a novel classification and identification algorithm for interchange injection based on Cassini CHEMS 3–220 keV $H^+$ energetic ions
- Radial occurrence rates and maximum partial $H^+$ pressure in interchange peaked between 7 and 9 Saturn radii for all intensity categories
- Occurrence rates peak on the nightside (1800–0600 LT) as compared to the dayside (0600–1800 LT)

**Correspondence to:**
A. R. Azari,
azari@umich.edu

**Citation:**
Azari, A. R., Liemohn, M. W., Jia, X., Thomsen, M. F., Mitchell, D. G., Sergis, N., et al. (2018). Interchange injections at Saturn: Statistical survey of energetic $H^+$ sudden flux intensifications. *Journal of Geophysical Research: Space Physics*, *123*, 4692–4711. https://doi.org/10.1029/2018JA025391

Received 24 FEB 2018
Accepted 3 MAY 2018
Accepted article online 9 MAY 2018
Published online 15 JUN 2018



**Abstract** We present a statistical study of interchange injections in Saturn's inner and middle magnetosphere focusing on the dependence of occurrence rate and properties on radial distance, partial pressure, and local time distribution. Events are evaluated from over the entirety of the Cassini mission's equatorial orbits between 2005 and 2016. We identified interchange events from CHarge Energy Mass Spectrometer (CHEMS) $H^+$ data using a trained and tested automated algorithm, which has been compared with manual event identification for optimization. We provide estimates of interchange based on intensity, which we use to investigate current inconsistencies in local time occurrence rates. This represents the first automated detection method of interchange, estimation of injection event intensity, and comparison between interchange injection survey results. We find that the peak rates of interchange occur between 7 and 9 Saturn radii and that this range coincides with the most intense events as defined by $H^+$ partial particle pressure. We determine that nightside occurrence dominates as compared to the dayside injection rate, supporting the hypothesis of an inversely dependent instability growth rate on local Pedersen ionospheric conductivity. Additionally, we observe a slight preference for intense events on the dawnside, supporting a triggering mechanism related to large-scale injections from downtail reconnection. Our observed local time dependence paints a dynamic picture of interchange triggering due to both the large-scale injection-driven process and ionospheric conductivity.

**Plain Language Summary** Studying high-energy particles around magnetized planets is essential to understanding processes behind mass transport in planetary systems. Saturn's magnetic environment, or magnetosphere, is sourced from a large amount of low-energy water particles from Enceladus, a moon of Saturn. Saturn's magnetosphere also undergoes large rotational forces from Saturn's short day and massive size. The rotational forces and dense internal mass source drive interchange injections, or the injection of high-energy particles closer to the planet as low-energy water particles from the inner magnetosphere are transported outward. There have been many strides toward understanding the occurrence rates of interchange injections, but it is still unknown how interchange events are triggered. We present a computational method to identify and rank interchange injections using high-energy particle fluxes from the Cassini mission to Saturn. These events have never been identified computationally, and the resulting database is now publically available. We find that the peak rates of interchange occur between 7 and 9 Saturn radii and that this range coincides with the highest intensity events. We also find that interchange occurrence rates peak on the nightside of Saturn. Through this study, we identify the potential mechanisms behind interchange events and advance our understanding of mass transport around planets.

## 1. Introduction

The Cassini spacecraft routinely observed interchange injection events with multiple instruments since arriving at Saturn in 2004. Interchange injection events are thought to arise from a Rayleigh-Taylor like plasma instability driven by Saturn's rapid rotation (period ~10.8 hr) and the dense plasma population that is created from Enceladus' plume neutrals. Strong centrifugal forces associated with the planetary rotation and internal neutral mass source from Enceladus result in a magnetosphere unstable to interchange (Hill, 1976; Michel & Sturrock, 1974; Southwood & Kivelson, 1987; Vasyliūnas, 1983). The centrifugal force causes swapping

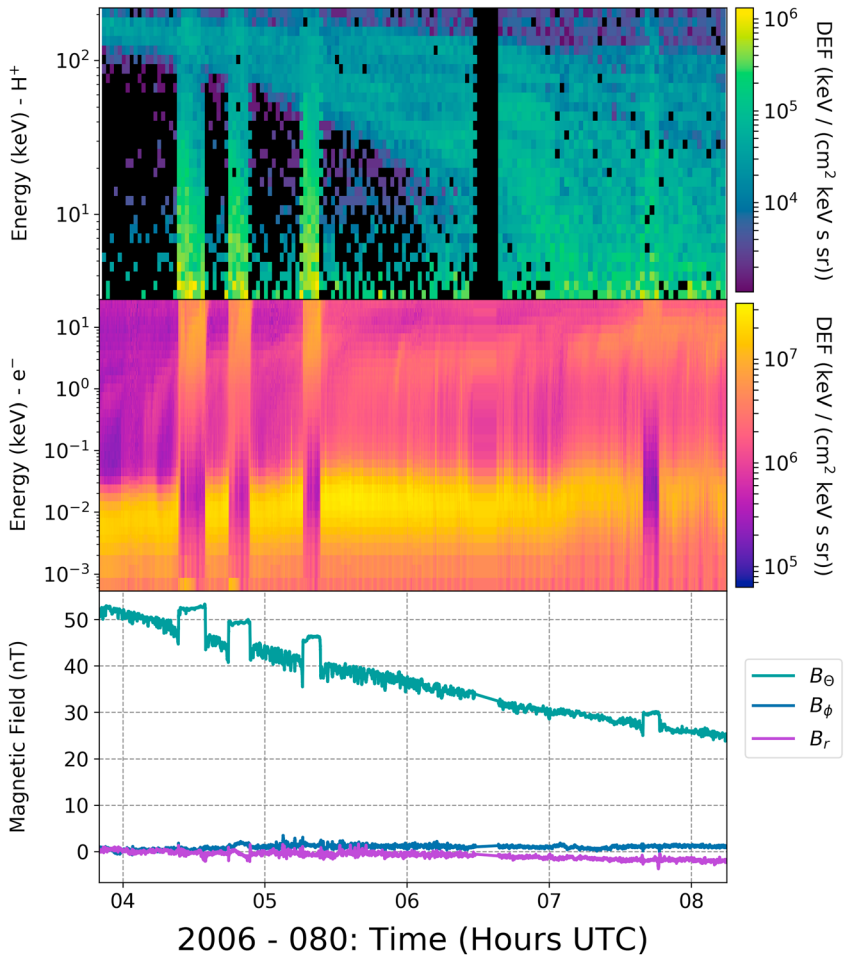


**Figure 1.** Series of interchange injections on 2006 day of year 080. The top plot is the differential energy flux of $H^+$ as measured by CHEMS between 3 and 220 keV, followed by the CAPS ELS differential energy flux for electrons from Anode 4, and finally the magnetic field in KRTP (Kronocentric body-fixed, J2000 spherical coordinates).

between magnetic flux tubes containing dense and cold plasma originating in the inner magnetosphere and the relatively depleted flux tubes farther out, whereby dense, cold plasma is slowly transported outward and less dense, hotter plasma is injected inward (e.g., Achilleos et al., 2015; Mauk et al., 2009; Thomsen, 2013). Such events are the primary source of mass transport in the inner/middle magnetosphere and play a critical role in plasma transport and dynamics within the Saturnian magnetosphere. Continuously supplied dense plasma must be transported outward, and to conserve magnetic flux, rapidly inward moving flux tubes of low density, energetic (>keV) plasma from the outer reaches of the Saturnian system also occur. These inward bound flux tubes are referred to as interchange injections. Since the arrival of Cassini at Saturn in 2004, interchange events have been observed with multiple sensors and thought to be the primary form of plasma transport from the inner magnetosphere to the outer magnetosphere (André et al., 2005, 2007; Burch et al., 2005; Hill et al., 2005; Mauk et al., 2005; Rymer et al., 2009; Thomsen et al., 2014).

In terms of particle measurements, an inward moving interchange flux tube is normally characterized by its intensification of hotter plasma (>100 eV) and depletion of cold plasma (see Figure 1). The variations in plasma pressure often lead to measurable changes in the magnetic field consistent with injections being in pressure balance with the surrounding plasma. As such, interchange injection events can also be identified in magnetic field data (André et al., 2005, 2007; Lai et al., 2016). Compared to interchange events, larger scale flux transport events occur predominantly within the night and morning sectors lending credence to their relation to reconnection processes (Müller et al., 2010). It is probably true that events that occur on larger spatial scales carry with them a population of energetic charged particles, for example, in excess of hundreds of keV (Mitchell et al., 2009; Paranicas et al., 2007). It has been shown to be less likely for spatially localized

(small) interchange to transport particles of hundreds of keV great distances inward, due to a drift out effect. In which, energetic particles are preferentially lost due to their larger gradient-curvature drifts and exit the interchange structures as compared to lower energy, or 1 keV particles (Burch et al., 2005; Paranicas et al., 2016). While these large-scale injections are often discussed in relation to post-reconnection-driven transport, their association with the more ubiquitous small events is still a point of research for small-scale interchange injections. For example, is a noticeable difference between triggering these large-scale events and smaller-scale events? Or can small-scale and large-scale events be thought of as a continuum? We know, for instance, that plasma must be shed, so the question is what magnetospheric factors, if any, lead to situations where heavy inner flux tubes are destabilized.

It has been suggested that after the occurrence of a large-scale injection, interchange occurrence rates would increase due to the enhanced flux tube gradient from the incoming plasma (Mitchell et al., 2015). This has been confirmed at a distance of ~8.6 $R_s$ to form a plasmapause with observed interchange injection activity (Thomsen et al., 2015). Within this paper, we will refer to interchange injections as "interchange" and tail-related processes as "large-scale injections."

Attempts to investigate interchange's dependence on other magnetospheric processes and plasma particle populations have resulted in several statistical survey analyses of the spatial dependence including radial and local time. Interchange occurs most often between at least 5 and 11 $R_s$, although not uncommonly extending beyond 11 $R_s$ (e.g., Chen & Hill, 2008; Thomsen, 2013, and references within) with a peak radial occurrence of ~8.5 Saturn Radii ($R_S$; Kennelly et al., 2013). By examining injections in Cassini Plasma Spectrometer (CAPS) data for the first two years of data after Saturn arrival, Chen and Hill (2008) found preferential occurrence rates in the prenoon sector; however, their method of identification excludes very young ($<$1 hr old) events. A statistical survey by Kennelly et al. (2013) based on Radio and Plasma Wave Science (RPWS) identified injections from 2004 to 2011 targeted specifically young fresh events via enhanced wave activity associated with the contained hot electrons; finding that the youngest interchange injections are preferentially located in the near-midnight and postnoon sector. Kennelly et al. (2013) accredits this difference to uncertainties associated with the back tracing method Chen and Hill (2008) used in calculating the injection locations. The discrepancy in local time location has caused uncertainty in what if any local time distributions of injections exist, and the relation of interchange to plasmoid release downtail through reconnection or other triggering processes. These surveys have not been extended to the later years of the Cassini mission. But since CAPS returned no data after mid-2012, surveys have to rely on other data sets.

The intensification of 3–220 keV $H^+$ within interchange injection events has not previously been used as an identification method for a statistical survey of local time or radial distributions. A working definition of interchange events, let alone a detailed understanding of physical process, is not agreed upon in literature. This is due to the wide variety of methods pursued in event identification, gaps in survey results, and resultant disagreements in local time distribution. By pursuing a statistical survey of high-energy plasma measurements over the entirety of the Cassini mission, we can complete the measurement set of Cassini observations related to interchange. Utilizing ion flux enhancement as our main identification criterion also allows us to observe different levels of intensification regimes and answer—of whether greater intensification events show different occurrence rates as compared to low intensification events.

We present an automated identification of interchange events using the Magnetosphere Imaging Instrument's (MIMI) CHarge Energy Mass Spectrometer (CHEMS) ion intensity data (Krimigis et al., 2004). CHEMS has near-continuous coverage during the Cassini mission, and pursuing the high-energy enhancement provides an opportunity to calculate particle pressure and intensity. We classify events by particle intensity increase above background flux levels and compare this new survey to previously published statistical interchange surveys to address the observed differences in these surveys. Such a computational classification and identification effort has never been pursued with ion intensity data, and we present similarities and differences to previous surveys.

We then evaluate interchange occurrence rates by local time and radial location, pressure, and intensity to answer our primary questions in this work: (1) do trends in local time and radial position persist over all phases of the mission/seasons of the planet and (2) are larger scale injections and ionospheric conductivity from the nightside of the planet playing a significant role for interchange occurrence rates?

## 2. Methods

### 2.1. Data

CHEMS obtains ion data by admitting a narrow energy per charge range into the device, then measuring the time of flight and energy deposited in the solid-state detector. The additional coincidence provided by the solid-state detector measurement is not available for all of the data (Krimigis et al., 2004). CHEMS has three separate telescope look directions each covering 53° in polar angle along the spacecraft's *z* axis, so it is often possible to sample different portions of the pitch angle distribution including measuring intensities near 90° pitch angle. For this reason we use CHEMS rather than the MIMI Low Energy Magnetospheric Instrument (LEMMS) instrument, as our primary energetic ion sensor as LEMMS is stuck since early 2005 at a single look direction and may not be sampling near 90° pitch angle as often as CHEMS. In addition, LEMMS's lowest energy for ions is 30 keV above our interest range between 3 and 22 keV. LEMMS is also sensitive to light contamination, making LEMMS difficult to use in an automated detection method (Vandegriff et al., 2013).

The sampling of CHEMS data utilized in this study is at no less than an ~2 min cadence. The sampling varies due to optimize for data quality and count rate. Inbound injections are represented in CHEMS $H^+$ data as a significant enhancement of energetic ions compared to the number local to the spacecraft without an injection event (Mauk et al., 2005). Inbound flux tubes are believed to come from a range of starting distances (Paranicas et al., 2016; Rymer et al., 2009). We expect the $H^+/W^+$ ratio to be significantly higher than background values in the inner magnetosphere (Thomsen et al., 2014).

We use this energetic $H^+$ enhancement between 3 and 22 keV as the main identification criterion in our methodology. This measurement range is fortuitous because the highest energies in these discrete events tend to be in the tens of keV. This range allows for the classification of events by intensity, where we classify the most intense enhancements as the most severe. Dispersion signatures from older events and large-scale injections are seen to dominate spectrograms predominantly above 20 keV as compared to fresh event signatures, and this is an additional limiting factor for our energy range selection (see Figure 1).

In Figure 1 we present a selected grouping of interchange injection events. This series of events is of particular interest due to the bevy of previous studies on the pitch angle distributions, transport, and morphology of these interchange events (Mitchell et al., 2015; Paranicas et al., 2016; Rymer et al., 2009). In particular, this event shows particle energization dependence upon pitch angle (Mitchell et al., 2015). In this work we focus on all pitch angles, and we present in Figure 1 a comparison of CHEMS $H^+$ differential energy flux for all pitch angles sampled, the thermal electrons as measured through the CAPS electron spectrometer (ELS), and magnetic field from the MAG instrument. This figure demonstrates the flux dropout discussed in the introduction within the thermal plasma and the intensification of the high-energy electrons, ions, and enhancement of magnetic field. The dispersion signatures discussed can be seen as the long curve in the CHEMS panel seen superimposed on the four fresh events. Our designed algorithm picks up each of these four fresh events, even though the fourth injection is particularly weak in CHEMS compared to the previous three.

We restrict our search for interchange events in the CHEMS $H^+$ data to the radial distances between 5 and 12 $R_s$, within the primary range of interchange occurrence rather than current sheet collapse events (Chen & Hill, 2008; Mitchell et al., 2015; Thomsen, 2013). This satisfactorily avoids any effects from the warping of the plasma sheet with varying solar wind attack angle, which can reach up to ±26.7° at solstice (e.g., Arridge et al., 2008, 2011; Carbary et al., 2008, 2015; Krimigis et al., 2007; Sergis et al., 2011, 2017). Additionally, we limit our analysis to equatorial locations over the course of the mission, restricting the survey within 10° of the equatorial plane in the Saturn Equatorial System (SZS) to constrain our results to the plasma disk to allow for a buildup of background statistics within this dense region. We use CHEMS $H^+$ data primarily from equatorial passes of Cassini from between 2005 to mid-2016, excluding the beginning of the mission in 2004 and several high-latitude passes from the later months of the mission. These limitations still give us reasonable sample sizes from CHEMS $H^+$ data to test and run our identification criteria with a total of 68,090 data points totaling ~172,980 minutes of sampling (see Figure 2).

In Figure 2 we present a diagram of Saturn by radial location and local time showing the total time the spacecraft spent in each location, after accounting for the restrictions described above on the CHEMS data set. The region between 5 and 12 $R_s$ is reasonably well sampled, but by restricting our data to near equatorial (i.e.,

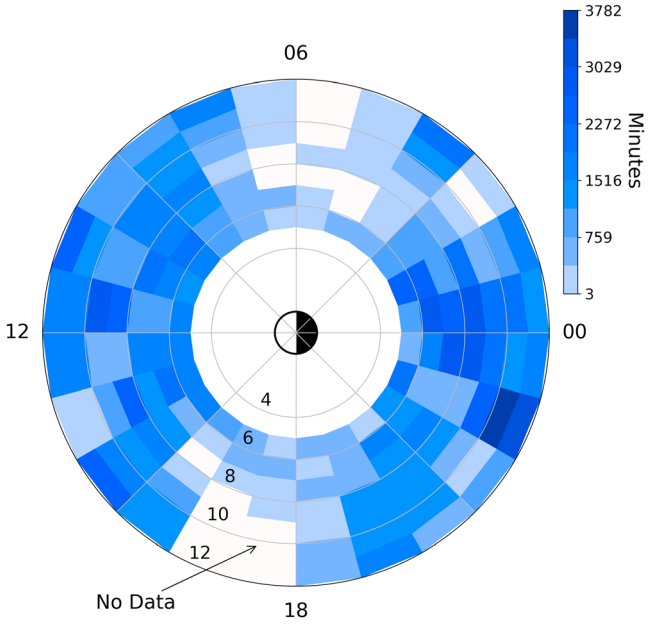


**Figure 2.** Spacecraft dwell time from 2005 to 2016 representing the sample size of the CHEMS $H^+$ data set. Each region shows the total minutes occupied by Cassini that satisfy our selection criteria. This figure demonstrates the dwell time calculated from CHEMS timestamps of the Cassini spacecraft within the radial range of 5–12 $R_s$ and at latitudes below 10° in SZS arranged by local time where noon is on the left of the figure. Bins with no data are shown in gray.

within 10° off the SZS equator), there are some gaps in local time, notably in the predusk and predawn sector. This is the primary rationale for presenting our results normalized to spacecraft dwell time to avoid sampling bias in our results.

We have designed and optimized an algorithm to automatically identify and rank events by $H^+$ particle intensity above the background plasma intensity. Additionally, this allows for a standardization of event identification and identification of categories of interchange intensity. This is extremely advantageous as we analyze the causation of the most intense interchange events as compared to less intense events and their respective influence from large-scale injection events. We discuss the algorithm development in sections 2.2 and 2.3.

### 2.2. Event Identification Procedure

The primary purpose of our designed algorithm is to identify, with reliability, and rank by their intensity, interchange events within the CHEMS $H^+$ equatorial data set between 2005 and 2016. Several critical design considerations were taken into account when developing this method, with the most critical being the distribution of plasma populations between 5 and 12 $R_s$. The Cassini trajectory had a range of periapsis distances and inclinations characterized by different particle populations. We address this by limiting our sampling to the primary region of interchange injection as discussed above, but additionally, we subset our data set by season and then we weight high intensity values with respect to their radial and energy ranges as described in the flowchart of Figure 3.

Figure 3 represents a visual description of our algorithm procedure. Our identification method starts subsetting the equatorial CHEMS $H^+$ data between 5 and 12 $R_s$ and partitioning into seasonal ranges of preequinox (2005–2008), equinox (2009–2011), and postequinox (2012–2016).

There is evidence in the Cassini data set of seasonal variations so we pursued this subset in our methodology to allow for any seasonal effects to be captured in our analysis and in our results (Sergis et al., 2011). We also observed by dividing the data set in this manner our algorithm performance improved. Down sampling further into smaller time ranges (by year for example) did not produce significant improvement. Additionally, these ranges contain roughly equal data sampling with ~760, 1,100, and 1,020 hr of data in the preequinox, equinox, and postequinox date ranges above, providing a roughly equal sampling for our *z*-score calculations (number of standard deviations above the mean or standard score as known within statistics). Our preequinox data set is slightly smaller, but this is because of a small number of low inclination orbits in the preequinox date range. Our choice of these date ranges was influenced by the natural data gaps in the equatorial data between years and to achieve similar sample sizes and location coverage between the three partitions while still increasing performance. We use these samples to build up an average with statistics and deviations from these averages through identification of outliers discussed in the next paragraph.

We further subset our seasonally separated data into 1 $R_s$ bins between 5 and 12 $R_s$ for the analysis as represented in Figures 3a–3c to address the variation in $H^+$ suprathermal plasma background with radial distance demonstrated in, for example, Sergis et al. (2017). Then for each 1 $R_s$ subset within each seasonal selection, we calculate the distribution of intensity values by energy range. This results in multiple distributions representing each season, radial location, and energy range between 3 and 22 keV. Using these distributions (see Figure 3b for an example distribution), we assign a *z*-score for each energy level between 3 and 22 keV (14 channels) for each CHEMS data point. This allows for addressing of any energy specific dependence within our data set by normalizing the value compared to the background (see Navidi, 2015). The *z*-scores are then summed and weighted as follows to obtain the variable *S* calculated in equation (1).

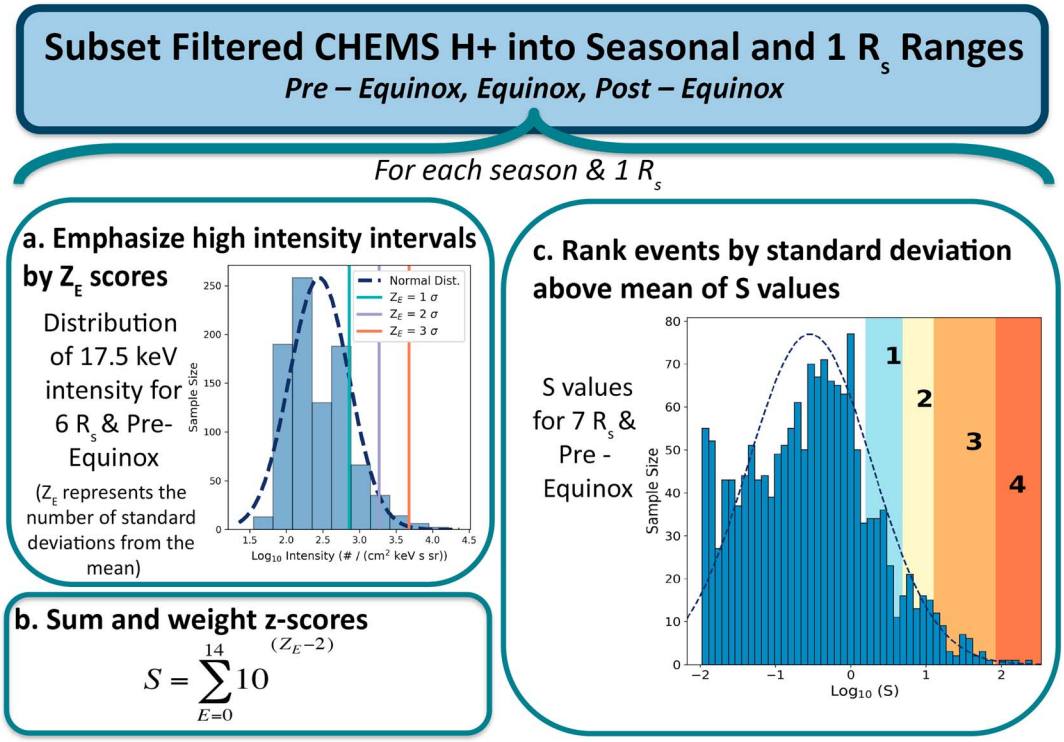


**Figure 3.** Diagram of CHEMS $H^+$ based event identification method. Within this diagram we present the algorithm procedure for event identification and seasonal subsetting procedure. (a) The plot is the distribution of the 17.5 keV data for 6–7 $R_s$ within the preequinox date range. Each line represents standard deviations above the mean, known as a *z*-score in statistics, with the first line representing 1 σ and so on. $Z_E$ is the *z*-values. (b) The equation summarizes how to obtain the dimensionless *S* value using the $Z_E$ scores obtained from panel (a). In which the $Z_E$ values are summed for each energy channel to obtain *S*. (c) An example *S* value distribution for 7–8 $R_s$ and the respective category breakdown from 1 to 4 with four representing the most extreme outliers. Even categories are shown in the highlighted colors ranging from smallest intensity in pale blue, to largest intensity in red.

$$S = \sum_{E=0}^{14} 10^{(Z_E-2)} \tag{1}$$

When *S* exceeds 0.9 standard deviations above the mean of *S*, then we consider this to be an interchange injection event. We call 0.9 the threshold value. Within equation (1), there are two values, which can be adjusted: (1) the *S* base multiplier—currently set to 10—will highlight extreme intensity values and scale *S* and (2) the *Z* power multiplier—currently set to 1—is applied to the $(Z_E - 2)$ as an exponentiation; this also will highlight extreme values. The current subtraction of 2 off of $Z_E$ is for ease of calculation and does not have an effect on the classification of events. Subtracting 2 moves the lower bound of *S* values for positive *z*-scores close to 0, rather than 1. For example, a *z*-score of 0 (or a mean value) results in summing values close to 1 ($10^0 = 1$), whereby subtracting by 2, we now sum values close to 0 ($10^{-2} = 0.01$).

This expression (shown additionally in Figure 3b) was chosen through comparing various functional forms to a preselected training set of interchange injection events. We discuss the optimization of this formula in section 2.3. The advantages of this particular formula are as follows: (1) it highlights high intensity outliers through exponentiation of the *z*-values and (2) it allows for natural data gaps or low intensity values at some but not all of the energy channels through a sum. This allows for flexibility in our algorithm by allowing any combination of high intensity values between energy channels 0 to 14 to obtain a large *S* value. These *S* values at each radial location are then used to identify an event and provide a statistically dependent ranking of how severe (intense compared to background) each event is.

We define intensity categories based on the *S* distributions as follows: category 1 (threshold for our event) from 0.9–1.5 standard deviations above the mean of *S* (σ), category 2 from 1.5 to 2 σ, category 3 from 2 to 3 σ, and category 4 from 3 σ and above. As one might expect categories 1 and 2 represent the smallest

intensity of all events, while categories 3 and 4 represent the most intense. The *S* values are radially dependent so these categories are designed to be radially variable to address underlying plasma deviations with radial distance.

We show in Figure 4 an example orbital segment for day of year 66–71 of 2005, with identified interchange injection events of these four categories in CHEMS data. We have also included the corresponding magnetic field variations. Within this figure there are magnetic field variations with no associated identified injection because of the lack of enhanced intensity of high-energy particles. This can be seen in the inbound orbital panel around time 22:30 UTC where the event in question shows significant dispersion and a lower signal at the lowest energy levels between 3 and 22 keV. This event is likely aged and thus does not trigger our algorithm. Since our method focuses on the enhancement of the hot particles compared to their average population in the area and energy range, the algorithm most readily captures young events. Similarly, we see events in the outbound panel that show differences in magnetic field signature. This is potentially a region where the internal pressure balance within the incoming flux tube varies, and thus, the magnetic field signature varies.

As illustrated in Figure 4 there are several events in quick succession. Our methodology sufficiently separates these events through an additional review of every event over 10 min. If a decrease beyond a category threshold occurs within an event of greater than 10 min, then the larger event is reclassified as multiple short-duration events. This is most evident in the inbound panel around hour 23:00 UTC.

### 2.3. Identification Optimization Procedure

We chose to develop an automated identification method rather than a by-hand identification to both reduce human bias in interchange injection identification and to enable a flexible novel categorization of interchange injection events by intensity. We used confirmed interchange injection events in 2005 for our test and training sets. These events were selected from comparisons between the lists of Lai et al. (2016), Kennelly et al. (2013), and Chen and Hill (2008), and our own examination of CHEMS H+ intensity data. Combined, the training and test sets represent 10% of our available data set (7,375/68,090 unique time points). To prevent any bias in our selection of training set data, the test and training sets are created by randomly selecting half of the available 7,375 points for each set. We optimize our algorithm on the training set, and then use the test set to estimate the error of our methodology. By splitting our test and training sets, we to prevent any over fitting of the designed algorithm on our training set.

We optimized the form presented above in equation (1) through multiple iterations through the training set of events. For each time within the training set, we categorize the data point as event or nonevent manually and compare to the algorithm detection methods. This allows us to create a binary contingency table. The contingency table consists of four categories from comparing the predicted (algorithm determined) events to the true (by-hand identified) time periods as follows: hits (H), misses (M), false positives (F), and true negative (N). Hits are defined as both the algorithm and our by-hand set identify an event; misses are when the algorithm does not identify an event, but the by-hand set does; false positives are when our algorithm identifies an event, while our by-hand set does not identify one. Finally, negatives are when both the algorithm and the by-hand set do not contain events.

The algorithm's classification ability was then investigated using the Heidke Skill Score (HSS), the probability of detection (POD), and the probability of false detection (PFD), which can be calculated from the contingency table values of H, M, F, and N, as follows (Heidke, 1926):

$$\mathrm{HSS} = \frac{2(\mathrm{HN} - \mathrm{MF})}{(\mathrm{H}+\mathrm{M})(\mathrm{M}+\mathrm{N}) + (\mathrm{H}+\mathrm{F})(\mathrm{F}+\mathrm{N})} \tag{2}$$

The HSS is a measure of correctly identified events compared to event predictions that are potentially correct from random chance. A perfect score is 1, while 0 indicates that the prediction is as good as random, and negative values denote worse than random (Heidke, 1926; Pulkkinen et al., 2013; Stephenson, 2000). For reference, current estimations of active space weather models for predicting ground dB/dt measurements are on average $<$0.5 HSS for different latitude ranges (Pulkkinen et al., 2013). Similarly, evaluations of Inner Magnetosphere Particle Transport and Acceleration Model to nowcast electron fluxes have a maximum HSS of 0.17 (Ganushkina et al., 2015). Our selected algorithm has an HSS of 0.56 for the training set and 0.49 for the test set.

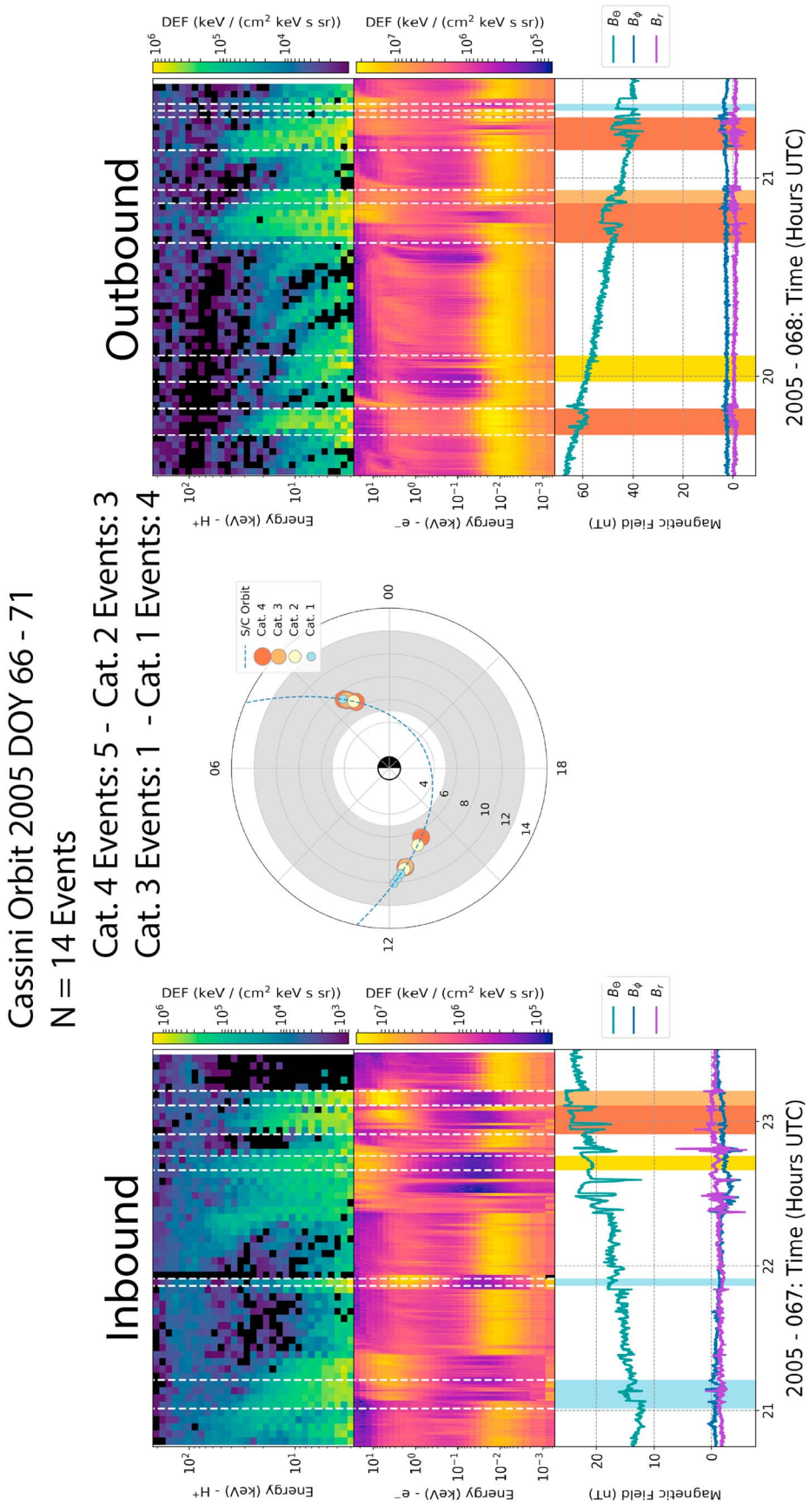


**Figure 4.** Cassini orbit pass and categorical events classifications identified for day of year (DOY) 66–71 of 2005. This figure demonstrates the different categories of events within one orbit pass in the beginning of 2005. The panels marked inbound and outbound represent selected portions of a single orbit trajectory, with the top subpanel displaying CHEMS H+ differential energy flux between 3 and 220 keV, followed by the CAPS ELS differential energy flux for electrons from Anode 4, and finally the magnetic field components in KRTP (Kronocentric body-fixed, J2000 spherical coordinates). We did not use the MAG or ELS data to identify events but we do display it here for illustration purposes. In the outbound panel we can observe how injection events may or may not show a demonstrated magnetic field enhancement. The middle panel represents the orbit of Cassini, with the region allowable for the algorithm shaded in grey. The orbit of Cassini is the blue dashed line plotted in local time in hours and radial distance in units of Saturn radii. In the orbit and magnetic field plots the most intense events are marked with dark orange, with least intense in light blue. In the CHEMS and CAPS panels the event boundaries are marked with dashed white lines.

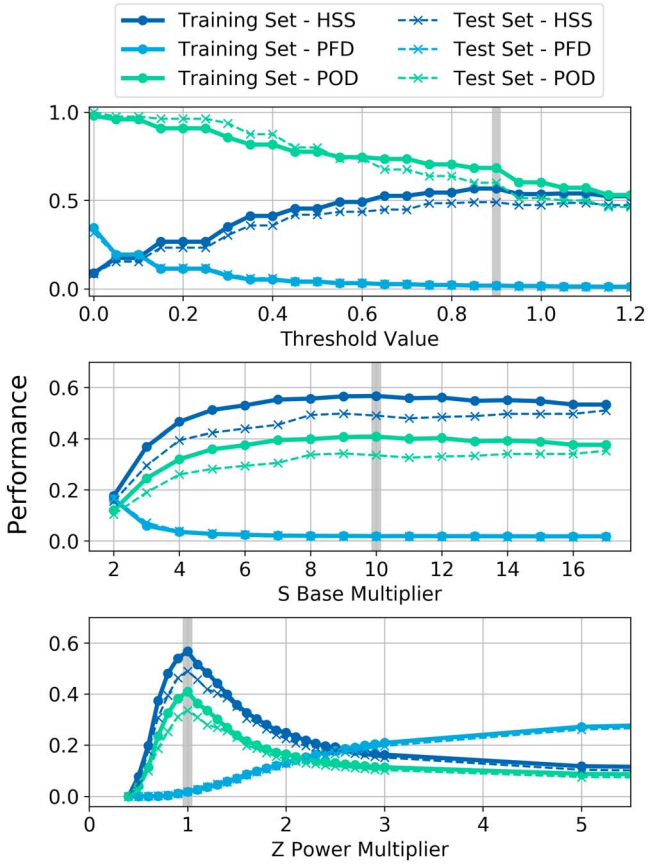


**Figure 5.** Performance curves of algorithm for varying values of controlling parameters. These curves were created by holding the other two parameters constant at their optimized values of 0.9 for the threshold value, 1.0 for the *Z* power, and 10 for the *S* base while varying the singular selected parameter. The grey shaded region represents the chosen variable value for the finalized algorithm**.** The *y* axis represents the performance, or the value of HSS, POD, and PFD. The solid lines with circles represent the performance evaluated for the training set, while the dashed lines with cross markers represent the performance of the test set. The first panel represents the threshold value, with the best HSS found at 0.9, highlighted in grey. The second panel plots the *S* base multiplier. There is negligible improvement after a value of 10. The third panel displays the *Z* power multiplier, which shows the best performance at a value of 1 for HSS.

The POD represents the fraction of actual events that were correctly identified (Pulkkinen et al., 2013). POD ranges from 0 to 1 with 1, representing no misses. When calculating POD it is important to consider it in relation to the trade-offs with the PFD. A perfect POD is 1, but in addition, there could be many false positives.

$$\mathrm{POD} = \frac{\mathrm{H}}{\mathrm{H} + \mathrm{M}} \tag{3}$$

The PFD represents the fraction of incorrectly identified nonevents (Pulkkinen et al., 2013). Similar to POD, it ranges from 0 to 1, but in this case, 0 represents a perfect score. It can be thought of as the inverse of specificity (1 - specificity), with 0 being the most specific.

$$\mathrm{PFD} = \frac{\mathrm{F}}{\mathrm{F} + \mathrm{N}} \tag{4}$$

We performed a multivariate analysis of performance by varying all three parameters, in essence creating a meshgrid of algorithm parameters. We found that upon this volume the maximum performance occurred while holding the other two parameters at their respective peak values and varying only one parameter. Figure 5 shows these maximum performance curves. The set of criteria used in our final algorithm was based on maximizing the HSS while minimizing the PFD. To optimize equation (1), we tested a range of values for the (1) threshold value above which the data set constitutes an event (set at 0.9 σ mean of S), (2) the *S* base multiplier, and (3) the *Z* power multiplier. The panels shown in Figure 5 represent the performance of the event identification method compared to both the training (solid) and the test (dashed) sets. As expected, the test set shows slightly lower performance but similar shape and peak behavior. This demonstrates that the algorithm is not over fitted to the training set but reliable over a wide range.

In Figure 6 we present the receiver operating characteristic (ROC) curves for the three selected parameters presented above (threshold value, *S* base multiplier, and *Z* power multiplier). In order to create an ROC curve we vary a parameter in our algorithm form and compare each output's PFD against the POD. This curve can be used to evaluate the performance of the algorithm form we designed and our chosen values by assessing its position on Figure 6, with the ideal position being in the upper left corner represented with 1 for the POD and 0 for the PFD, that is, a perfect classification. We designed our classifier algorithm to be limited in terms of the worst possible prediction and by maximizing our HSS; thus, our curve does not venture into the upper right corner of only false positives. Similarly, we opted to limit as much as possible the detection of false positives at the expense of detecting all possible events when choosing parameter values, as can be seen in the location of the grey shaded dots, which represent the final values chosen. Ideally, a classifier algorithm should be located above the grey dashed line as this represents random chance in ROC space (e.g., Fawcett, 2006; Mason, 1982, and references within). Because our chosen algorithm values product PODs significantly below the maximum sensitivity, it can be thought of as a conservative estimation of interchange as it has a high threshold of event identification to reduce false positives in our resultant set.

We examined our false positives from both the training and the test sets for any systematic errors that would affect our conclusions not covered in our previous methodology. We did not find any systematic errors in our local time distribution. However, by radial distance, there is a larger proportion of false positives beyond 11 $R_s$. We attribute this to the changing plasma population beyond 11 $R_s$ from thermal, cool plasma of the inner magnetosphere to the less dense energetic plasma of the outer magnetosphere and where our methodology begins to identify more high intensity events, which are not attributed to interchange (e.g., Schippers et al.,

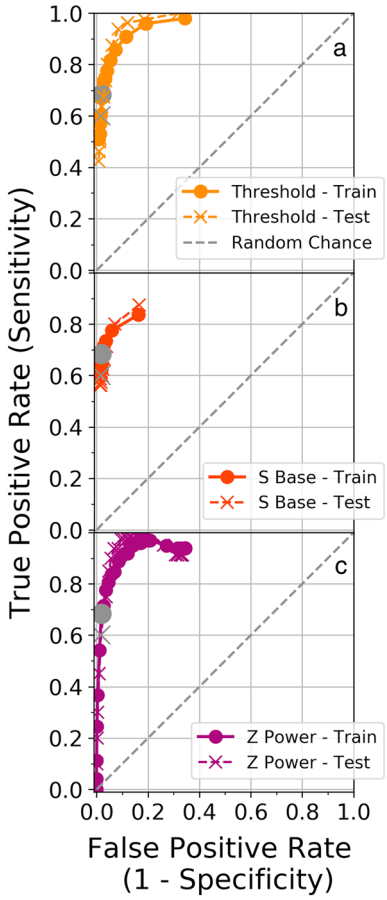


**Figure 6.** ROC curves of varying algorithm values. These curves were created by holding the other two parameters constant at their optimized values of 0.9 for the threshold value, 1.0 for the *Z* power, and 10 for the *S* base while varying the singular selected parameter. The panels shown here represent the performance of the event identification method compared to both the training (solid) and the test (dashed) sets. The grey shaded values represent the chosen variable value for the finalized algorithm**.** All chosen values result in a less sensitive, but more specific algorithm. (a) ROC curve for threshold value. (b) ROC curve for *S* base multiplier. (c) ROC curve for Z power values.

2008; Thomsen et al., 2015). When analyzing our results we constrain our conclusions to be based only on the survey results between 5 and 10 $R_s$ but we present the survey results beyond 10 $R_s$ for comparative purposes. This methodology represents the first implementation of a classification algorithm developed for interchange events based on energetic particle data.

## 3. Results

We identified 816 interchange injections over the course of the Cassini mission between 2005 and 2016, 256 in the preequinox period (2005–2008), 303 in the equinox period (2009–2011), and 257 in the postequinox period (2012–2016). The following sections analyze the occurrence of these events compared to previous surveys (section 3.1), in radial location (section 3.2), and in local time (section 3.3).

### 3.1. Comparison to Lai et al. (2016), Kennelly et al. (2013), and Chen and Hill (2008)

Over the course of the Cassini mission, several large statistical studies have been conducted looking at the occurrence rates of interchange injection events. Each survey, however, focuses on investigating interchange from the viewpoint of one instrument. Lai et al. (2016), for example, examined the magnetic field data focusing on the enhancement and depletion of magnetic field pressure associated with the pressure balance of tangential discontinuities (see Figure 4 for demonstrated magnetic field perturbations). Kennelly et al. (2013) focused on the plasma wave emissions associated with interchange such as the upper hybrid emission, electron cyclotron harmonics, and whistler mode emissions. Chen and Hill (2008), on the other hand, focused on CAPS ELS data. Because of these restrictions, and our particular focus on the high-energy $H^+$ particles of MIMI CHEMS, we do not expect a one-to-one matching between event lists. Rather, we investigate the similarity of these studies to our own, recognizing that all studies examine different physical changes manifested in interchange injection events.

To run a comparison between event lists, care must be taken to limit it to only those events that are eligible. For example, all studies vary in the range of dates, time resolution, spatial location, and methodology. We address this by limiting comparisons to events that occur within the same date and spatial range. This is most restrictive to the Lai et al. (2016) due to their additional examination of higher latitudes (i.e., off the magnetospheric equator). An event is counted as a match between lists if there is any overlap in identified time stamps. This is required to compare studies as the time resolution between chosen methodology varies—often with multiple MAG identified events located inside plasma data identified events. This is additionally why a one-to-one matching is not plausible where events in our study can match to more than one event in others and vice versa. This restricts our comparison-eligible events from 816 to 663, mostly due to the extension of our study to the postequinox range.

In Figure 7 we present previous statistical studies compared to our identified list. We represent our comparison using the Circos tool more commonly used in genomics research (Krzywinski et al., 2009). This tool enables easy visualization of relational data wherein two objects are connected to each other in varying quantities especially when the data set in question has multiple characteristics. We find that our survey shares ~30% of its events (187/663) with any of the lists of Lai et al. (2016), Kennelly et al. (2013), or Chen and Hill (2008). Of these 187 events ~55% belong to category 3/4 and a slightly smaller amount, ~46%, to category 1/2 events.

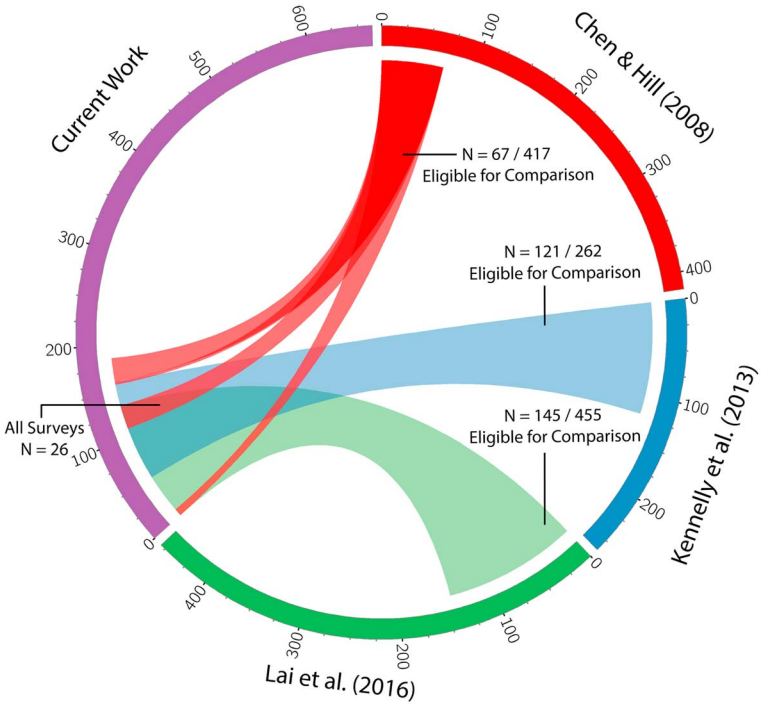


**Figure 7.** Comparison between injection events identified in the current presented study from MIMI CHEMS $H^+$ data and events identified in statistical surveys from Lai et al. (2016), Kennelly et al. (2013), and Chen and Hill (2008). The size of the ribbons connecting the nodes (colored arcs) represents the number of similar events between our list and others. Chen and Hill (2008) is represented with three ribbons to illustrate the shared overlap with other surveys. The ribbons are proportional to the number of shared events.

Of these 187 events, only 26 events are found shared between all of the event lists, including the current work. The remaining events (476) are primarily low intensity category 1/2 events (~72%), while high intensity category 3 and 4 events represented only ~28% of the unique-to-our-survey 476 events. We confirm that the most intense interchange events (higher categories) correlate between different instrument observations at higher rates than those of lower intensity.

Kennelly et al. (2013) has the most comparable list to that of our own, with 46% of their eligible comparison events finding a match within our list (121/262), followed by Lai et al. (2016) with ~30% (145/455), and Chen and Hill (2008) with ~14% (67/417). This can be seen as the ribbons in Figure 7 leading to the nodes of the previous studies. About 187 unique events in total can be found in our list with matches in previous surveys. These consist of the following represented as the ribbons leading to the current node:

- 110 can be found within Kennelly et al. (2013).
- 135 can be found within Lai et al. (2016).
- 63 can be found within Chen and Hill (2008).
- 8 can be found within Chen and Hill (2008) and Lai et al. (2016).
- 84 can be found within Kennelly et al. (2013) and Lai et al. (2016).
- 26 can be found within Kennelly et al. (2013), Lai et al. (2016), and Chen and Hill (2008).
- 2 can be found within Kennelly et al. (2013) and Chen and Hill (2008).

We will be discussing the implications of this range in the following section. Our event list therefore captures a large percentage of Kennelly et al. (2013), but this only comprises a small part of our own list (~30%)—confirming that while many of our events are unique, we reliably find previous studies.

We further compared our study to previous work by examining the partial particle pressure from interchange events from MIMI CHEMS $H^+$ between 3 and 22 keV, the primary region we used to identify interchange. To

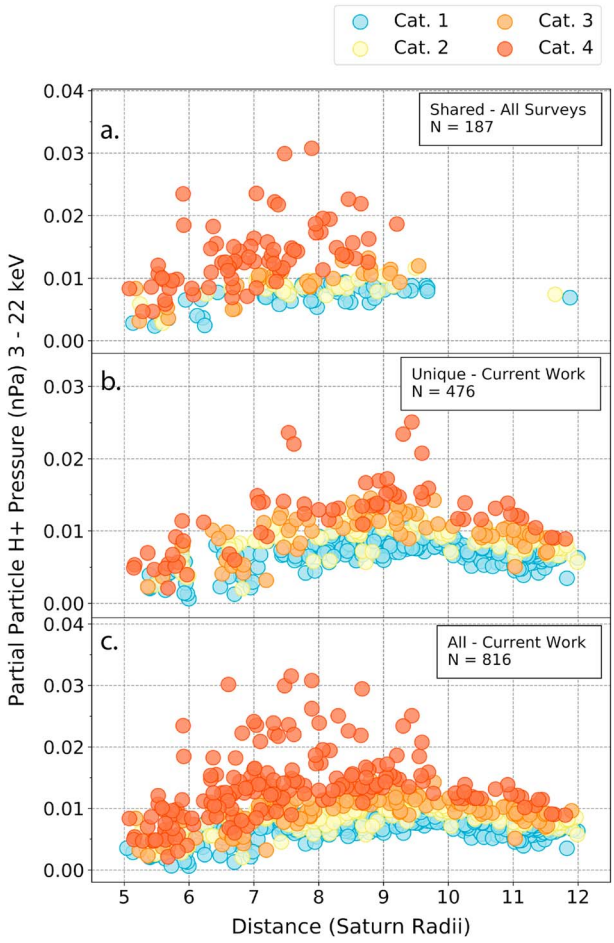


**Figure 8.** Comparison of identified event partial particle pressure (3–22 keV H+) to previous surveys. (a) Partial particle pressure of interchange events cross listed in all surveys. This panel contains all cross-listed events, totaling 187 in total. (b) Partial particle pressure of interchange events only found in current work. This panel contains all of our events that could be compared, but are not found within another list (476 events). (c) Partial particle pressure of interchange events of all events in current work. This panel contains all of our events (816 total).

calculate the partial pressure from $H^+$ within our selected energy range, we used the methodology outlined in Krimigis et al. (1981) and additionally expanded on in Sergis et al. (2007).

In Figure 8 we present the partial particle pressure distribution of $H^+$ between 3 and 22 keV for interchange injection events shared between our list and previous lists, and those unique only to our study. The pressures presented corresponds to the maximum reached pressure within the interchange event. This does not include $W^+$ group contribution but rather focuses on the physical quantity selected for our classification scheme.

As seen by a comparison of Figures 8a and 8b, the events within our list which are shared between studies and those unique to our study are of similar distribution. By comparing these panels, we see immediately that category 1 events are less likely to be shared between studies than events in categories 2, 3, and 4. Events with highest maximum partial pressure peak within the 6–9 $R_s$ radial range. They do not, however, continue into 5 $R_s$, and these interchange events tend to cluster within 6–9 $R_s$, whereas other categories of events (lower pressures) are distributed over a wider range of radial distance with no clear peak. Event categories are based on particle pressure at each radial distance separately, thus becoming smaller nearer to Saturn, generally following the known suprathermal pressure profile (e.g., Sergis et al., 2017, and references within). We calculate the mean values of partial pressure for categories 1–4 within picopascals (pPa):

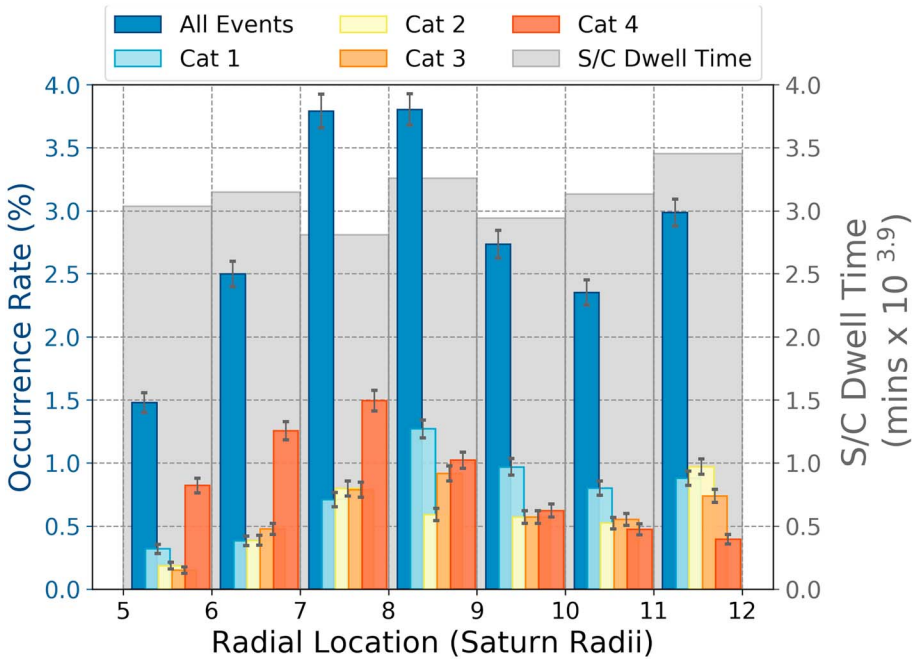


**Figure 9.** Radial distribution of interchange events from 2005 to 2016. Superimposed on the total sampling time the spacecraft spent in each radial bin of 1 $R_S$ (the grey shaded region), we demonstrate by category of event the occurrence rates of interchange (the colored bars). We have binned our data by 1 $R_S$ to prevent any sampling bias. Each bar plotted represents a 1 $R_S$ range. The dark blue bars represent all categories combined.

- Category 1: 7.1 ± 0.1 pPa
- Category 2: 8.3 ± 0.2 pPa
- Category 3: 9.7 ± 0.2 pPa
- Category 4: 13.5 ± 0.4 pPa

Within these means the errors are the standard error on the mean. The categories by pressure are distinct from each other, as their mean and standard errors do not overlap. We also find that the chosen algorithm form is able to capture the changes in background plasma population successfully. The gap region between 10 and 12 $R_S$ is due to our limitations in cross comparing Chen and Hill (2008) and Kennelly et al. (2013) as these surveys ended at 10 $R_S$ and 11 $R_S$, respectively.

### 3.2. Radial Occurrence

We investigate the radial distribution of interchange injection between 5 and 12 $R_S$ by overall occurrence rate and by intensity category. In Figure 9 we demonstrate the normalized occurrence (time spent within an injection event/total observation time by spacecraft within region) by radial location for the whole survey range, regardless of seasonal partitioning. We did not observe any significant deviation in radial location with season. As expected we observe a peak occurrence rate in the 7–9 $R_S$ region from all our events, with 8–9 $R_S$ demonstrating a slightly higher occurrence rate. This is similar to previous surveys, which find a peak around 8.5 $R_S$ (Kennelly et al., 2013). By category, however, we observe our most intense events peak at 7 $R_S$ while less intense events (categories 1 and 2) peak further out at 8–9 $R_S$ and 11–12 $R_S$, respectively. As mentioned before, at 11 $R_S$ we see the greatest occurrence of false positives, and thus, we do not conclude trends using this range. As discussed in section 2, 11 $R_S$ is known to contain a large amount of false positives due to the large amount of highly energetic plasma and other tail-related processes. The secondary peak at 11 $R_S$ we attribute to category 2 events and the presence of false positives beyond 11 $R_S$.

The peaks between 7 and 9 $R_S$ can also be seen in our partial pressure distributions in Figure 8. In reviewing Figure 8 we note that our lower pressure events show less variation with in radial location, and in fact, the highest-pressure events show a distinctly different radial occurrence pattern than that of the bulk of events of lower pressure.

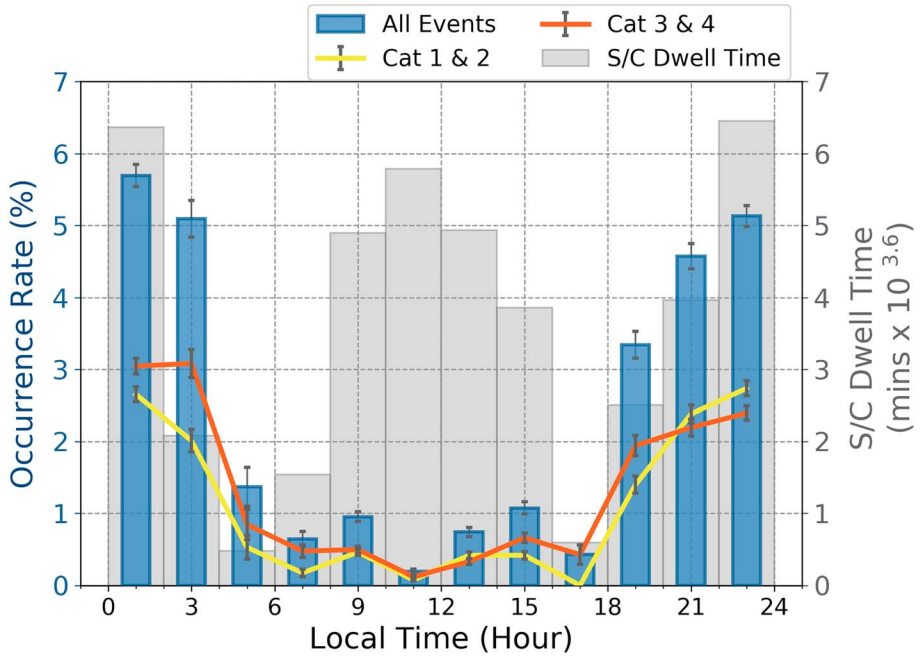


**Figure 10.** Local time distribution of interchange injection events over all years from 2005 to 2016. Superimposed on the total sampling time that the spacecraft spent in each local time bin of 2 hr (the grey shaded region), we present by grouped category of interchange the occurrence rates (time in event/total observation time) as a function of local time (blue bars and colored lines). The blue bars represent all interchange injections, while the yellow and orange lines represent the rates of low intensity (categories 1 and 2) and high intensity (categories 3 and 4), respectively.

### 3.3. Local Time Occurrence

We examined the local time occurrence rates of interchange in order to resolve current disagreements in local time occurrence rates from Chen and Hill (2008) and Kennelly et al. (2013) and to evaluate interchange occurrence rate dependence on large-scale injection events. In Figure 10 we present all event occurrence rates from 2005 to 2016. The occurrence rates are calculated from the total time spent in an interchange event divided by the total time spent observing within that location. The error bars calculated here and in the following figures are representative of the sampling error of $1/(\text{sample size})^2$. The error bars therefore increase in size when we have low representative samples or low event statistics.

Between 2005 and 2016 we observe a strong day-night asymmetry with a majority of events accounted for on the nightside of the planet ranging from ~5 to 6 times higher occurrence rates. The dayside distribution in Figure 10 can be seen symmetrically located around noon with peaks in the prenoon and postnoon sectors with the lowest occurrence rates located at noon. This is most similar to Kennelly et al. (2013) due to the nightside dominance, but we find both the prenoon (0900) peak reported in Chen and Hill (2008) and the postnoon peak (1500) reported in Kennelly et al. (2013). Additionally, we observe a slightly higher occurrence rate of more intense events (categories 3 and 4) on the dawnside of Saturn. We additionally investigated the local time distribution in our preassigned seasonal date ranges of preequinox, equinox, and postequinox. We find that in all of these ranges, the nightside occurrence rates far dominate over the dayside occurrence rates.

### 3.4. Duration and Scale Size

We find that of the events identified, the majority are less than 15 min long (769 of 816 events or 94%). In Figure 11 we present the normalized distribution of durations of all identified events. The lower limit in event duration is due to CHEMS time resolution, and it is likely that there are events occurring below our observed cutoff. Shorter events are more commonly thought of as interchange, with fewer long (>15 min) events generally occurring at larger radial distances (Chen et al., 2010; Thomsen et al., 2014). Our distribution is supported by previous studies evaluating the duration of magnetic field signatures of interchange events (Lai et al., 2016).

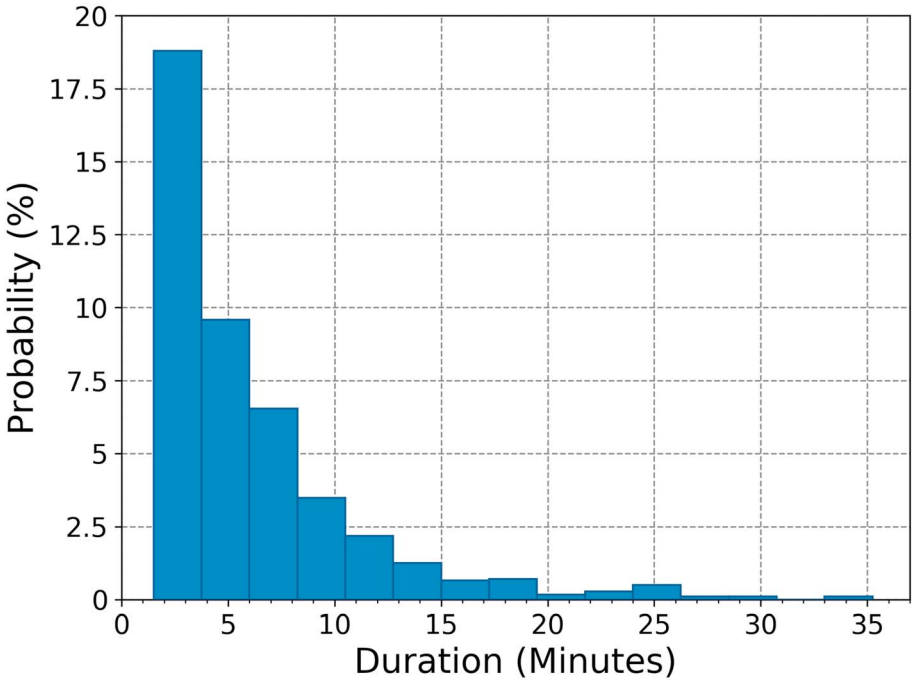


**Figure 11.** Normalized distribution of interchange event duration. The normalized event distribution by duration is presented for all events (all intensity categories). There are 15 bins ranging from the lowest instrument resolution of ~2 min to the longest event of ~34 min.

Based on the event durations, we calculated an estimated width of the interchange injection events. As the velocities of corotating particles in addition to their gradient-curvature drifts are much larger than the spacecraft velocity itself, we assume that the interchange event overtakes the spacecraft. Similar to the methodology employed in Chen et al. (2010), we calculate the scale size of the interchange structure with equation (5). In which we find the width in $R_s$ ($W$) by multiplying the average radial location in $R_s$ (60,268 km) of the interchange structure ($R$) by the duration in seconds, by the angular frequency of $H^+$ plasma at the location in radians/second ($\Omega$). The angular frequency is obtained from the mean $H^+$ azimuthal flow velocities obtained in Thomsen et al. (2010); which surveyed the bulk ion parameters from the CAPS instrument, deriving estimates of the azimuthal flow velocities usually between ~50 and 70% of solid corotation. This survey only extends to 6 $R_s$; to calculate the velocities of interchange events between 5 and 6 $R_s$ we use estimated values at 6 $R_s$.

$$W = R\,\Delta T\,\Omega \tag{5}$$

We find that low intensity events are statistically smaller than high intensity events. Category 1 and 2 interchange structures (low intensity) have a mean width of 0.25 $R_s$, and category 3 and 4 (high intensity) events have a mean width of 0.41 $R_s$. The widths range from ~0.04 to 1.72 $R_s$. We include the interchange widths (see the Acknowledgments section) material along with error ranges propagated from the standard error on the mean azimuthal velocities included in Thomsen et al. (2010).

We additionally find a nightside/dayside asymmetry in the duration with long events (>15 min) more likely to be found on the nightside than on the dayside. We identified only 2 events on the dayside (out of 117 dayside events) >15 min long, while there were 45 events on the nightside (out of 699 nightside events) >15 min long.

## 4. Discussion

### 4.1. Comparison to Lai et al. (2016), Kennelly et al. (2013), and Chen and Hill (2008)

In comparing our survey to published statistical surveys, we were careful to limit comparisons to the same date and space as discussed in section 3.1. We cannot, however, remove the influence from each survey's

primary instrument identification choice and therefore do not expect interchange event lists to compare exactly to each other. We did find a greater correlation between previous surveys' events to high $H^+$ intensity interchange in our own. We suggest that these events would have a greater chance of being observed by each survey as suggested by Chen and Hill (2008) as the decrease of low energy plasma observed by CAPS would potentially be more intense, by Lai et al. (2016) in MAG from an increase in resultant magnetic field signature from the depletion of low energy plasma, and by Kennelly et al. (2013) in enhanced plasma wave activity due to perturbations in the electron density. Future work should analyze these instruments in aggregate to analyze these potential dependences. Additionally, we designed our identification criteria for high intensity events, but still gather lower intensity events, so it is not unexpected to find this result. What is surprising, however, is the variation of our comparison to different surveys and subsequent small number of events found in all four lists.

We have found only 26 events to be correlated between all these lists. While this is limited to only events that can be compared, this is still a small subset of events. Additionally, our own survey correlates most highly with Kennelly et al. (2013) as compared to the surveys by Lai et al. (2016) and Chen and Hill (2008). In the case of Chen and Hill (2008) we attribute this difference to their study's focus on events of $>1$ hr old while the other surveys reviewed optimized for younger events. We attribute the greater match with Kennelly et al. (2013) as compared to the survey by Lai et al. (2016) to similarities in event identification criteria. Our event identification requires a substantial increase of $H^+$ flux intensity above the average background. Kennelly et al. (2013) identified events through particular focus on the strength of signatures of upper hybrid waves, secondary plasma waves, and perturbations in the electron cyclotron frequency. We are curious as to the significant overlap between our surveys given our event criteria. Lai et al. (2016) identified interchange on the equatorial plane through enhancements in magnetic field over the background that had a significant rise within a set time period. We expect their survey to contain events that might not have the plasma enhancement within the CHEMS energy range evaluated (3–22 keV) here. The potential differences between these surveys can also be observed in the presentation of CHEMS, CAPS, and MAG data within Figures 1, 4, and 7.

Given the differences we have identified between published surveys to our own, however, we find such comparisons to be useful in evaluating the physical processes behind interchange injection events. There is a significant amount of interchange we observe only in certain measurements and not within others. This suggests that the underlying observation or occurrence mechanisms behind what we identify as interchange vary. Our analysis has not looked into comparisons between previous works, only comparisons of those works to our own. To fully evaluate the differences, we would need to compare each survey to each other, and this is not the focus of the present work. Additionally, our study has not evaluated contributions from $W^+$ or other ion species besides $H^+$ as this is the main species we expect to see in incoming interchange events (Thomsen et al., 2014). Future work should consider the effect of additional criteria for both identification and for comparison of pressure within interchange events and between lists in order to address the underlying differences in the observed events.

### 4.2. Radial Occurrence

We observe the greatest occurrence of interchange to be located between 7 and 9 $R_s$ which is a slightly more expanded range than the single peak at 8.5 $R_s$ from Kennelly et al. (2013). We attribute this to the increased range of events we consider as compared to previous surveys. This location also coincides with the greatest observed partial high-energy $H^+$ pressure in events as discussed previously. Thus, we find that not only do events occur more frequently within this range but also the events that are most intense occur within this range.

The outer end of this range at 9 $R_s$ correlates well with the location of a plasmapause-like boundary that separates incoming low density flux tubes arriving from reconnection processes downtail and inner magnetosphere rotating dense plasma (Thomsen et al., 2015). This boundary exhibits a large gradient in flux tube content, one of the major triggering processes of interchange signatures, and signatures were indeed observed to be forming in the event reported by Thomsen et al. (2015). We suggest that due to energization accompanying inward radial motion (e.g., within injection) competing with charge-exchange losses, the population of 3–22 keV protons maximizes between 7 and 9 $R_s$. This result confirms interchange's role as a major radial transport mechanism for high energy particles between 6 and 9 $R_s$, as previously discussed by DeJong et al. (2010), Thomsen et al. (2016), and Hill (2016).

### 4.3. Local Time Occurrence

We find in section 3.3 the local time distribution from 2005 to 2016 that the interchange occurrence rate is ~5–6 times higher on the nightside (1800–6 LT) than on the dayside (0600–1800 LT), supporting a significant potential triggering mechanism located on the nightside of Saturn. A similar nightside preference was observed by Kennelly et al. (2013), but they also observed a significant postnoon peak in occurrence rates. We expect the growth rate of the instability to inversely depend on the local Pedersen ionospheric conductivity (Southwood & Kivelson, 1987). We propose therefore that as the nightside ionosphere would have a low conductivity, the local growth rates on the nightside would be higher than those on the dayside. So while the initiation does not depend on the conductivity, interchange will become more unstable and more detectable on the nightside.

Müller et al. (2010) identified 52 electron injection events observed with the MIMI LEMMS instrument. They back traced dispersed injection events to their original local time location, which shows heavy nightside dependence with a slightly higher postnoon dayside sector. Our detection criterion is based on the lowest levels (0–14) of CHEMS or between ~3 and 22 keV. We observe younger and lower energy events than Müller et al. (2010) but see a significant similarity to their local time results with a much larger sample size.

We also observed a slightly higher occurrence of intense events in the dawn sector (0000–0600). It is worth pursuing in a future work if there are noticeable differences between high intensity events in the dawn sector as compared to other sectors. Previous work has attributed interchange triggering to incoming flux tubes from large-scale injections, setting up the necessary flux tube content gradient as proposed by Mitchell et al. (2015) and demonstrated in the case study by Thomsen et al. (2015) mentioned above. Statistically, this preference seems small if existent, and it would be worth pursuing additional event studies within this region as compared to others.

In this analysis we focused on observation of injection events at the locations observed, rather than adjusting for the possibility of local time offsets due to both Coriolis force and finite radial propagation speed in order to compare to previous work. However, such effects can potentially adjust the local time location of interchange injection dependent on the inflow speed (Liu et al., 2010; Paranicas et al., 2016). Future work should investigate possible adjustments to the local time distributions in this and previously performed surveys.

### 4.4. Duration and Scale Size

We find the vast majority of events identified last for 15 min or less. This supports the idea of interchange as a process occurring in a narrow region (~5–10%) of available longitude space as proposed and discussed in Chen and Hill (2008). Additionally, our distribution of duration is very similar to that of Lai et al. (2016) with the bulk of interchange events occurring on a short time scale.

We additionally observed a nightside asymmetry in duration (see section 3.4). The is in addition to a higher occurrence rate of nightside interchange events. As both the duration and the occurrence rates peak on the nightside suggesting that the nightside is the region with more intense and frequent interchange events.

From these durations, we calculated the width, finding that there is a difference in widths between category 1 and 2 interchange structures (low intensity) and category 3 and 4 (high intensity) structures. We suggest that this is an observed effect of a larger intensity of events also resulting in larger scale sizes from the growth of the instability. These estimates have been updated from Chen et al. (2010) by including the azimuthal velocity profile from Thomsen et al. (2010).

Our overall range between ~0.04 and 1.72 $R_s$ agrees with interchange injections as a "mesoscale" structure, limited to below many $R_s$ (Hill et al., 2005). The mean estimated width and radial distribution for category 1 and 2 events of 0.25 $R_s$ appears to be in the distribution within Chen et al. (2010). The lower limit is approximately half of that reported within Hill et al. (2005). Hill et al. (2005) limited to observing interchange signatures with a clear dispersal; this is the most likely cause for the disagreements between these surveys as well as the updated azimuthal rotational profile from Thomsen et al. (2010). It is possible that as an interchange event sweeps over Cassini, the spacecraft only observes a part (random cross-section) of the event, not indicative to its true size. This limitation should be considered in further work to evaluated event size.

## 5. Conclusions and Future Work

We have presented a novel method for identification and classification of interchange events based on the intensity of the 3–22 keV $H^+$ from CHEMS. The automated algorithm was robustly trained and tested to optimize selection of young injection events and is the first automated particle based classification algorithm developed for interchange injections. We have compared our survey to previous statistical surveys and investigated the dependences of the occurrence rate and partial particle pressure on the radial distance, local time, and season. We have found the following:

1. Interchange occurrence rates peak between 7 and 9 $R_s$, and the maximum 3–22 keV partial pressure injections are limited to 6–9 $R_s$.
2. Local time occurrence rates of interchange between 2005 and 2016 are highest on the nightside and show slight preference for higher intensity events on the dawnside. This suggests a combined influence of the ionospheric conductivity in determining the growth rate of interchange instability and the large-scale tail reconnection in injecting hot and depleted flux tubes into the middle magnetosphere, which enhances the gradient in flux tube content relative to the inner magnetosphere.
3. Most injection events last for 15 min or less in duration with a small trend toward longer events on the nightside rather than the dayside. Smaller intensity events have a mean width of 0.25 $R_s$, and high intensity events have a mean width of 0.41 $R_s$.
4. A comparison of events between this and three previous surveys showed relatively high overlap for some and low overlap with others, which can be explained by considering the selection criteria and the instrumentation used for each study. A surprising finding was the very small percentage of events (26 events) that were common to all four survey lists.

Our work has found that energetic proton injections are strongly organized by local time and radial distance. Future work should further investigate the underlying triggering mechanisms of interchange and how these influence plasma mass and transport within the Saturnian system. Further investigations should include study of the occurrence by different periodic fluctuation-based longitude systems such as the Saturn longitude systems and planetary period oscillation systems (e.g., Gurnett et al., 2011; Provan et al., 2016, and references within). Periodicities in the plasma properties and magnetic field have been observed at periods closely related to those of the emission power of Saturn kilometric radiation, leading to the hypothesis that the process controlling Saturn kilometric radiation modulation also controls aspects of magnetospheric physics (e.g., Carbary & Mitchell, 2013, and references within). Previous works have disagreed on interchange organization by longitude, and updating these results with this data set would be worthwhile (Chen et al., 2010; Chen & Hill, 2008; Kennelly et al., 2013). If interchange is organized within planetary oscillation phase, then interchange is a process propagating periodicities between the inner and outer magnetosphere of Saturn and should be investigated in future work.

**Acknowledgments**
The authors are grateful to Tom Hill, Hairong Lai, Martha Kusterer, and colleagues at the University of Michigan including Alicia Schooley, Camilla Harris, Ryan Dewey, Kenneth Hansen, and Jenna Wiens for insights and suggestions to improve this study. The authors appreciate work done in identifying Saturn injections by the International Space Science Institute team "Modes of radial plasma motion in planetary systems". Cassini CHEMS data used within this study and Cassini MAG data and Cassini CAPS data displayed in our figures may be found online at the NASA Planetary Data System (PDS). A. Azari would like to thank the Michigan Space Grant Consortium, the Michigan Institute for Plasma Science and Engineering, the NASA Earth and Space Science Fellowship Program grant NNX15AQ63H, and the NSF Graduate Research Fellowship Program under grant DGE 1256260. Additional support for Michigan coauthors came from NASA under grants NNX15AH28G, 80NSSC17K0015, and NNX17AB87G. Work at the University of Iowa was supported by NASA through contract 1415150 with the Jet Propulsion Laboratory (JPL). M. F. Thomsen was supported by the NASA Cassini program through JPL contract 1243218 with Southwest Research Institute. Our survey results and comparison to previous works are located on the Deep Blue Data Repository under doi:10.7302/Z2WM1BMN or can be received through e-mail contact with A. Azari.

## References

Achilleos, N., André, N., Blanco-Cano, X., Brandt, P. C., Delamere, P. A., & Winglee, R. (2015). 1. Transport of mass, momentum and energy in planetary magnetodisc regions. *Space Science Reviews*, *187*(1–4), 229–299. https://doi.org/10.1007/s11214-014-0086-y

André, N., Dougherty, M. K., Russell, C. T., Leisner, J. S., & Khurana, K. K. (2005). Dynamics of the Saturnian inner magnetosphere: First inferences from the Cassini magnetometers about small-scale plasma transport in the magnetosphere. *Geophysical Research Letters*, *32*, L14S06. https://doi.org/10.1029/2005GL022643

André, N., Persoon, A. M., Goldstein, J., Burch, J. L., Louarn, P., Lewis, G. R., et al. (2007). Magnetic signatures of plasma-depleted flux tubes in the Saturnian inner magnetosphere. *Geophysical Research Letters*, *34*, L14108. https://doi.org/10.1029/2007GL030374

Arridge, C. S., André, N., Khurana, K. K., Russell, C. T., Cowley, S. W. H., Provan, G., et al. (2011). Periodic motion of Saturn's nightside plasma sheet. *Journal of Geophysical Research*, *116*, A11205. https://doi.org/10.1029/2011JA016827

Arridge, C. S., Khurana, K. K., Russell, C. T., Southwood, D. J., Achilleos, N., Dougherty, M. K., et al. (2008). Warping of Saturn's magnetospheric and magnetotail current sheets. *Journal of Geophysical Research*, *113*, A08217. https://doi.org/10.1029/2007JA012963

Burch, J. L., Goldstein, J., Hill, T. W., Young, D. T., Crary, F. J., Coates, A. J., et al. (2005). Properties of local plasma injections in Saturn's magnetosphere. *Geophysical Research Letters*, *32*, L14S02. https://doi.org/10.1029/2005GL022611

Carbary, J. F., & Mitchell, D. G. (2013). Periodicities in Saturn's magnetosphere. *Reviews of Geophysics*, *51*, 1–30. https://doi.org/10.1002/rog.20006.1

Carbary, J. F., Mitchell, D. G., Paranicas, C., Roelof, E. C., & Krimigis, S. M. (2008). Direct observation of warping in the plasma sheet of Saturn. *Geophysical Research Letters*, *35*, L24201. https://doi.org/10.1029/2008GL035970

Carbary, J. F., Sergis, N., Mitchell, D. G., & Krupp, N. (2015). Saturn's hinge parameter from Cassini magnetotail passes in 2013–2014. *Journal of Geophysical Research: Space Physics*, *120*, 4438–4445. https://doi.org/10.1002/2015JA021152

Chen, Y., & Hill, T. W. (2008). Statistical analysis of injection/dispersion events in Saturn's inner magnetosphere. *Journal of Geophysical Research*, *113*, A07215. https://doi.org/10.1029/2008JA013166

Chen, Y., Hill, T. W., Rymer, A. M., & Wilson, R. J. (2010). Rate of radial transport of plasma in Saturn's inner magnetosphere. *Journal of Geophysical Research*, *115*, A10211. https://doi.org/10.1029/2010JA015412

Dejong, A. D., Burch, J. L., Goldstein, J., Coates, A. J., & Young, D. T. (2010). Low-energy electrons in Saturn's inner magnetosphere and their role in interchange injections. *Journal of Geophysical Research*, *115*, A10229. https://doi.org/10.1029/2010JA015510

Fawcett, T. (2006). An introduction to ROC analysis. *Pattern Recognition Letters*, *27*(8), 861–874. https://doi.org/10.1016/j.patrec.2005.10.010

Ganushkina, N. Y., Amariutei, O. A., Welling, D., & Heynderickz, D. (2015). Nowcast model for low-energy electrons in the inner magnetosphere. *Space Weather*, *13*, 16–34. https://doi.org/10.1002/2014SW001098

Gurnett, D. A., Groene, J. B., Averkamp, T. F., Kurth, W. S., Ye, S.-Y., & Fischer, G. (2011). An SLS4 longitude system based on a tracking filter analysis of the rotational modulation of Saturn kilometric radiation. *Planetary Radio Emissions*, *VII*, 51–64. https://doi.org/10.1553/PRE7s51

Heidke, P. (1926). Berechnung des Erfolges und der Güte der Windstärkevorhersagen im Sturmwarnungdienst (Calculation of the success and goodness of strong wind forecasts in the storm warning service). *Geografiska Annaler Stockholm*, *8*, 301–349.

Hill, T. W. (1976). Interchange stability of a rapidly rotating magnetosphere. *Planetary and Space Science*, *24*(12), 1151–1154. https://doi.org/10.1016/0032-0633(76)90152-5

Hill, T. W. (2016). Penetraing of external plasma into a rotation-driven magnetosphere. *Journal of Geophysical Research: Space Physics*, *121*, 10,032–10,036. https://doi.org/10.1002/2016JA023430

Hill, T. W., Rymer, A. M., Burch, J. L., Crary, F. J., Young, D. T., Thomsen, M. F., et al. (2005). Evidence for rotationally driven plasma transport in Saturn's magnetosphere. *Geophysical Research Letters*, *32*, L14S10. https://doi.org/10.1029/2005GL022620

Kennelly, T. J., Leisner, J. S., Hospodarsky, G. B., & Gurnett, D. A. (2013). Ordering of injection events within Saturnian SLS longitude and local time. *Journal of Geophysical Research: Space Physics*, *118*, 832–838. https://doi.org/10.1002/jgra.50152

Krimigis, S. M., Carbary, J. F., Keath, E. P., Bostrom, C. O., Axford, W. I., Gloeckler, G., et al. (1981). Characteristics of hot plasma in the Jovian magnetosphere: Results from the Voyager spacecraft. *Journal of Geophysical Research*, *86*, 8227–8257.

Krimigis, S. M., Mitchell, D. G., Hamilton, D. C., Livi, S., Dandouras, J., Jaskulek, S., et al. (2004). Magnetosphere Imaging Instrument (MIMI) on the Cassini mission to Saturn/Titan. *Space Science Reviews*, *114*(1–4), 233–329. https://doi.org/10.1007/s11214-004-1410-8

Krimigis, S. M., Sergis, N., Mitchell, D. G., Hamilton, D. C., & Krupp, N. (2007). A dynamic, rotating ring current around Saturn. *Nature*, *450*(7172), 1050–1053. Retrieved from doi:https://doi.org/10.1038/nature06425

Krzywinski, M. I., Schein, J. E., Birol, I., Connors, J., Gascoyne, R., Horsman, D., et al. (2009). Circos: An information aesthetic for comparative genomics. *Genome Research*, *19*(9), 1639–1645. https://doi.org/10.1101/gr.092759.109

Lai, H. R., Russell, C. T., Jia, Y. D., Wei, H. Y., & Dougherty, M. K. (2016). Transport of magnetic flux and mass in Saturn's inner magnetosphere. *Journal of Geophysical Research: Space Physics*, *121*, 3050–3057. https://doi.org/10.1002/2016JA022436

Liu, X., Hill, T. W., Wolf, R. A., Sazykin, S., Spiro, R. W., & Wu, H. (2010). Numerical simulation of plasma transport in Saturn's inner magnetosphere using the Rice Convection Model. *Journal of Geophysical Research*, *115*, A12254. https://doi.org/10.1029/2010JA015859

Mason, I. (1982). A model for assessment of weather forecasts. *Australian Meteorological Magazine*, *30*(4), 291–303.

Mauk, B. H., Hamilton, D. C., Hill, T. W., Hospodarsky, G. B., Johnson, R. E., Paranicas, C., et al. (2009). Fundamental plasma processes in Saturn's magnetosphere. In M. K. Dougherty, et al. (Eds.), *Saturn from Cassini-Huygens* (pp. 281–331). Dordrecht: Springer Netherlands. https://doi.org/10.1007/978-1-4020-9217-6_11

Mauk, B. H., Saur, J., Mitchell, D. G., Roelof, E. C., Brandt, P. C., Armstrong, T., et al. (2005). Energetic particle injections in Saturn's magnetosphere. *Geophysical Research Letters*, *32*, L14S05. https://doi.org/10.1029/2005GL022485

Michel, F. C., & Sturrock, P. A. (1974). Centrifugal instability of the jovian magnetosphere and its interaction with the solar wind. *Planetary and Space Science*, *22*(11), 1501–1510. https://doi.org/10.1016/0032-0633(74)90015-4

Mitchell, D. G., Brandt, P. C., Carbary, J. F., Kurth, W. S., Krimigis, S. M., Paranicas, C., et al. (2015). Injection, interchange, and reconnection. *Magnetotails in the Solar System*, *2004*, 327–343. https://doi.org/10.1002/9781118842324.ch19

Mitchell, D. G., Carbary, J. F., Cowley, S. W. H., Hill, T. W., & Zarka, P. (2009). The dynamics of Saturn's magnetosphere. In M. K. Dougherty, L. W. Esposito, & S. M. Krimigis (Eds.), *Saturn from Cassini-Huygens* (pp. 257–279). Dordrecht: Springer Netherlands. https://doi.org/10.1007/978-1-4020-9217-6_10

Muller, A. L., Saur, J., Krupp, N., Roussos, E., Mauk, B. H., Rymer, A. M., et al. (2010). Azimuthal plasma flow in the Kronian magnetosphere. *Journal of Geophysical Research*, *115*, A08203. https://doi.org/10.1029/2009JA015122

Navidi, W. C. (2015). Statistics for engineers and scientists. *Statistics for Engineers & Scientists*. New York, NY: McGraw-Hill Education. Retrieved from https://mirlyn.lib.umich.edu/Record/014865504 CN-QA 276.4.N38

Paranicas, C., Mitchell, D. G., Roelof, E. C., Mauk, B. H., Krimigis, S. M., Brandt, P. C., et al. (2007). Energetic electrons injected into Saturn's neutral gas cloud. *Geophysical Research Letters*, *34*, L02109. https://doi.org/10.1029/2006GL028676

Paranicas, C., Thomsen, M. F., Achilleos, N., Andriopoulou, M., Badman, S. V., Hospodarsky, G., et al. (2016). Effects of radial motion on interchange injections at Saturn. *Icarus*, *264*, 342–351.

Provan, G., Cowley, S. W. H., Lamy, L., Bunce, E. J., Hunt, G. J., Zarka, P., et al. (2016). Planetary period oscillations in Saturn's magnetosphere: Coalescence and reversal of northern and southern periods in late northern spring. *Journal of Geophysical Research: Space Physics*, *121*, 9829–9862. https://doi.org/10.1002/2016JA023056

Pulkkinen, A., Rastätter, L., Kuznetsova, M., Singer, H., Balch, C., Weimer, D., et al. (2013). Community-wide validation of geospace model ground magnetic field perturbation predictions to support model transition to operations. *Space Weather*, *11*, 369–385. https://doi.org/10.1002/swe.20056

Rymer, A. M., Mauk, B. H., Hill, T. W., André, N., Mitchell, D. G., Paranicas, C., et al. (2009). Cassini evidence for rapid interchange transport at Saturn. *Planetary and Space Science*, *57*(14–15), 1779–1784. https://doi.org/10.1016/j.pss.2009.04.010

Schippers, P., Blanc, M., André, N., Dandouras, I., Lewis, G. R., Gilbert, L. K., et al. (2008). Multi-instrument analysis of electron populations in Saturn's magnetosphere. *Journal of Geophysical Research: Space Physics*, *113*, A07208. https://doi.org/10.1029/2008JA013098

Sergis, N., Arridge, C. S., Krimigis, S. M., Mitchell, D. G., Rymer, A. M., Hamilton, D. C., et al. (2011). Dynamics and seasonal variations in Saturn's magnetospheric plasma sheet, as measured by Cassini. *Journal of Geophysical Research*, *116*, A04203. https://doi.org/10.1029/2010JA016180

Sergis, N., Jackman, C. M., Thomsen, M. F., Krimigis, S. M., Mitchell, D. G., Hamilton, D. C., et al. (2017). Radial and local time structure of the Saturnian ring current, revealed by Cassini. *Journal of Geophysical Research: Space Physics*, *122*, 1803–1815. https://doi.org/10.1002/2016JA023742

Sergis, N., Krimigis, S. M., Mitchell, D. G., Hamilton, D. C., Krupp, N., Mauk, B. M., et al. (2007). Ring current at Saturn: Energetic particle pressure in Saturn's equatorial magnetosphere measured with Cassini/MIMI. *Geophysical Research Letters*, *34*, L09102. https://doi.org/10.1029/2006GL029223

Southwood, D. J., & Kivelson, M. G. (1987). Magnetospheric interchange instability. *Journal of Geophysical Research*, *92*, 109–116. https://doi.org/10.1029/JA092iA01p00109

Stephenson, D. B. (2000). Use of the "odds ratio" for diagnosing forecast skill. *Weather and Forecasting*, *15*(2), 221–232. https://doi.org/10.1175/1520-0434(2000)015%3C0221:UOTORF%3E2.0.CO;2

Thomsen, M. F. (2013). Saturn's magnetospheric dynamics. *Geophysical Research Letters*, *40*, 5337–5344. https://doi.org/10.1002/2013GL057967

Thomsen, M. F., Coates, A. J., Roussos, E., Wilson, R. J., Hansen, K. C., & Lewis, G. R. (2016). Suprathermal electron penetration into the inner magnetosphere of Saturn. *Journal of Geophysical Research, A: Space Physics*, *121*, 5436–5448. https://doi.org/10.1002/2016JA022692

Thomsen, M. F., Mitchell, D. G., Jia, X., Jackman, C. M., Hospodarsky, G., & Coates, A. J. (2015). Plasmapause formation at Saturn. *Journal of Geophysical Research, A: Space Physics*, *120*, 2571–2583. https://doi.org/10.1002/2015JA021008

Thomsen, M. F., Reisenfeld, D. B., Delapp, D. M., Tokar, R. L., Young, D. T., Crary, F. J., et al. (2010). Survey of ion plasma parameters in Saturn's magnetosphere. *Journal of Geophysical Research*, *115*, A10220. https://doi.org/10.1029/2010JA015267

Thomsen, M. F., Reisenfeld, D. B., Wilson, R. J., Andriopoulou, M., Crary, F. J., Hospodarsky, G. B., et al. (2014). Ion composition in interchange injection events in Saturn's magnetosphere. *Journal of Geophysical Research: Space Physics*, *119*, 9761–9772. https://doi.org/10.1002/2014JA020489.Received

Vandegriff, J., Difabio, R., Hamilton, D., Kusterer, M., Manweiler, J., Mitchell, D., et al. (2013). Cassini/MIMI instrument data user guide.

Vasyliūnas, V. M. (1983). Plasma Distribution and Flow. doi:https://doi.org/10.1029/2003JD004173.Aires